Published in final edited form as:

IEEE Biomed Circuits Syst Conf. 2022 October ; 2022: 439–443. doi:10.1109/biocas54905.2022.9948674.

Programmable Electrochemical Stimulation on a Large-Scale CMOS Microelectrode Array

Pushkaraj S. Joshi[†], **Kangping Hu**[†], **Joseph W. Larkin**[‡], **Jacob K. Rosenstein**[†]

[†]Brown University, Providence, RI, USA

[‡]Boston University, Boston, MA, USA

Abstract

In this paper we present spatio-temporally controlled electrochemical stimulation of aqueous samples using an integrated CMOS microelectrode array with 131,072 pixels. We demonstrate programmable gold electrodeposition in arbitrary spatial patterns, controllable electrolysis to produce microscale hydrogen bubbles, and spatially targeted electrochemical pH modulation. Dense spatially-addressable electrochemical stimulation is important for a wide range of bioelectronics applications.

Keywords

Microelectrode array; stimulation; electrolysis; bubble formation; pH control

I. Introduction

Microelectrode arrays have proven to be powerful and flexible platforms for interfacing with cultured cells and tissues. Many valuable applications have focused on classical electrophysiological responses from excitable cells, especially cardiac cells [1], [2] and neurons [3]–[10]. However, in addition to eliciting action potentials, patterned electrical stimulation can affect metabolism, change gene expression [11], modulate growth and immune response [12], and induce cell death [13], in both mammalian and bacterial cells [14]. Outside of applications involving living cells, microelectrode arrays can also use electrical stimulation to drive redox reactions and provide spatiotemporal control of local pH for molecular applications such as highly parallel DNA synthesis [15]–[17]. Stimulation with dense microelectrode arrays of course also pairs naturally with integrated sensing modes [8], [13], [18]–[24].

We have previously presented large-scale CMOS microelectrode arrays with integrated electrochemical impedance sensing and imaging features [18], [25]–[30], which we have applied for imaging single cells [27], detection and classification of microorganisms [25], and imaging biofilm growth [30]. Here we show how these arrays can be programmed for spatio-temporal electrical stimulation. We demonstrate gold electroplating in arbitrary spatial patterns, and use these functionalized arrays to drive electrolysis of water, producing localized hydrogen bubbles as well as microscale pH gradients.

II. Hardware Platform Design

A. Pixel and Electrode Array Design

The microelectrode array is integrated on a CMOS sensor with 131,072 pixels arranged in a 256 × 512 array. An image of the array architecture and a simplified pixel schematic are shown in Fig. 1. Each pixel contains SRAM cells which determine whether it operates in sensing mode or stimulation mode (Fig. 1(b)), allowing the array to be configured for stimulation with any arbitrary spatial pattern. In stimulation mode (Fig. 1(c)), the switches can be biased in the linear region for bipolar voltage stimulation, or biased as cascoded current sources for bipolar current stimulation. Stimulation polarity and timing are determined by external digital controls. Here we focus only on the voltage stimulation mode, while the other operating modes of the chip are described in [30].

B. Layout and Packaging

The circuits are implemented in 180 nm CMOS technology, and individual pixels are 10μm × 10μm with an exposed top metal electrode. The overall chip is 25 mm^2, with the electrode array occupying 13.1 mm^2 [30]. The chip is wirebonded to a small printed circuit board module, and the bondwires are encapsulated with epoxy, leaving the active array area exposed [31]. The module plugs into a custom data acquisition board hosting ADCs, DACs, power management, and an FPGA module (Opal Kelly XEM7310) with a USB interface.

III. Experimental Results

A. Electroplating of Gold

The pixels are initially fabricated using the aluminum top metal from the foundry, which is prone to oxidation and corrosion at moderate voltages in common aqueous buffers. We construct a small open fluid chamber around the sensor array with a polypropylene tube sealed with silicone adhesive. We then remove the aluminum layer in acid (Aluminum Etchant Type A, Transene), exposing the underlying tungsten vias and titanium nitride diffusion barrier layer. These materials are conductive and stable, and can be used as-is, but it can also be valuable to introduce other metals to the surface. We filled the chamber with 2 mL gold plating solution (SG-10, Transene), plus a small amount of surfactant (2 μL Triton-X100) to ensure complete wetting of the microscale pixels. A small vibrating dental plaque remover tip was used to agitate the solution and improve mixing, and the chip was positioned on a hotplate set to 75°C. The experimental setup is shown in Fig. 2.

The pixels to be electroplated are programmed with STIMU_EN=1 (as illustrated in Fig. 1(c)), and these pixels are pulsed between 1.8 V and 0 V using the on-chip switches. The pulse duration was 1 sec with 50% duty cycle. A stainless steel counter electrode is biased at 1.8 V. For the intervals of time when the stimulated pixels are at 0 V, they act as cathodes and gold ions in the plating solution are deposited on the pixels. The remaining pixels have STIMU_EN=0 and are held at 1.2 V, and do not receive any gold deposition.

In Fig. 3, we show electron microscope images of a 16 × 16 array of pixels after varying amounts of plating time (Zeiss LEO 1530 SEM). The electrodeposited gold at each pixel has

a large surface area, with sharp dendrites and multiple nucleation sites. Dendritic structures are expected for electroplating in cyanide baths carried out at high deposition potential and low pulse duration [33], [34]. The increased surface area would be expected to decrease the interfacial impedance and provide higher total stimulation current. The deposition potential used here is 1.8 V and t_{ON} is 0.5 sec. Based on these experiments, we selected t = 120 sec for gold electrodeposition. The in-pixel SRAM means that these electroplating protocols can be applied to arbitrary spatial patterns within the electrode array. For example, Fig. 4 shows gold selectively electroplated in a Sierpinski triangle fractal pattern.

B. Programmable Generation of Hydrogen Bubbles

Spatial control of gas evolution can be valuable for patterning cells on a microelectrode array surface [13]. In aqueous solutions, there is a relatively small window (≈ 1.23 V) of electrochemical stability, beyond which water molecules may become unstable. The electrolysis reaction at the cathode produces hydrogen gas as well as hydroxide ions:

$$2H_2O + e^- \rightarrow H_2 + 2[OH]^- \quad (1)$$

Due to the low solubility and low mass density of hydrogen gas in an aqueous solution, the hydrogen gas tends to coalesce and produce bubbles. To study the bubble formation on the CMOS array, we employed a PBS buffer (pH 7) with 50 mM KCl salt as the electrolyte. The gold-coated pixel surface was stimulated to act as a cathode, while a silver wire held at 1.8 V was used as the counter electrode. We observe rapid nucleation and growth of hydrogen gas over the stimulated area (Fig. 5). The growth rate of the bubbles depends on the spatial distribution of hydrogen, and its diffusion rates. The analytical solution to the unsteady growth of hydrogen bubble diameter (d) is expected to scale approximately with $\sqrt{t}$ as

$$d_t - d_0 = 4\beta\sqrt{D_H t} \quad (2)$$

where d_0 is the initial diameter, d_t is the diameter at time t, and D_H is the diffusivity of hydrogen in an aqueous solution ($\approx 10 \times 10^{-9}$ m^2/s). The parameter β represents the degree of hydrogen supersaturation. Monitoring the sizes of several bubbles (Fig. 6), we see that their growth fits well to Eq. 2. The fit value for the supersaturation parameter is $\beta = 0.13$. Since this experiment was performed using the fractal electoplated array, it is reasonable that β is slightly lower than typical values from the literature (0.22 – 0.63) [35], where electrolysis is usually carried out over a large uniform electrode surface. The experiment suggests that stimulation time < 1s could be enough to induce local cell detachment.

C. Spatially Controlled pH Modulation

Electrochemical modulation of local pH has been used to influence the viability of biofilms [36] as well as to support programmable DNA synthesis [16]. There are multiple parameters which affect generated pH gradients, including the stimulation mode (potentiostat versus galvanostat), redox chemistry, reservoir geometry, and stimulation time. Here, we utilize the [OH] radicals produced as a result of the electrolysis of water to modulate pH. The hydroxyl radicals will tend to react and disperse over time, and the extent of pH modulation

will depend on the number of excess [OH] radicals introduced, as well as their spatial confinement. Mass transfer at the pixel is described by the faradaic equation:

$$\text{moles of [OH] per pixel} = \frac{It}{zF} \tag{3}$$

where z is valence (the number of electrons consumed per [OH] produced), F is Faraday's constant, I is the stimulation current at each pixel, and t is the effective duration of stimulation. I is a function of the applied stimulation voltage, but in these experiments we generally do not measure the current directly. To monitor the spatio-temporal pH changes, we prepared an electrolyte consisting of DI water mixed with pH indicator dye (0.04% bromothymol blue plus $\approx$50 mM potassium chloride). The dye was orange-yellow at the initial pH ($\approx$5.5), and it turns blue at basic pH (> 7.4). Fig. 7 shows that within 1 second the pH begins to change near stimulated pixels. The dispersion of hydroxyl radicals beyond the stimulated pattern (Fig. 7 (e)) appears to initially follow a diffusion model ($L_D = 2\sqrt{Dt}$), but it soon transitions to an advection regime ($L_D = vt$), where L_D is the dispersion distance from the stimulated region, D is the diffusivity of hydroxyl ions in an aqueous solution ($\approx 5 \times 10^{-9}$ m^2/s), v is the advection velocity, and t is the time elapsed. We suspect that bubble generation creates recirculation currents of the hydroxyl radicals and speeds up the horizontal pH dispersion [37]. The typical vertical velocity of hydrogen bubbles due to electrolysis is in the range of 40,000 – 100,000 μm/sec [35]. We observe lateral dispersion which is faster than would be expected from diffusion alone, but which is still approximately two orders of magnitude slower than the vertical motion of microscale bubbles which detach from the surface. Slower dispersion is preferable when the aim is to stimulate a meaningful spatial pH gradient. Introducing redox couples such as hydroquionine [16], [17] could help to influence pH without bubble formation, although adding redox couples could also affect cell metabolism.

IV. Conclusion

We have presented programmable electrochemical stimulation using an integrated CMOS microelectrode array chip. These experiments build on earlier presentations of the sensing modalities of the platform. The underlying circuit architecture allows for independent configuration of each pixel, which we demonstrate by electroplating of a complex fractal pattern. We then applied these stimulation features for water hydrolysis including microscale hydrogen bubble generation and local pH modulation. In comparison to the other studies (Table I), this work demonstrates the voltage stimulation capabilities on the highest number of pixels and stimulation channels. Large-scale targeted stimulation is useful across a wide range of bioelectronics applications, and our ongoing research includes applying this system to study the effects of spatio-temporal electrochemical stimulation in bacterial biofilms.

Acknowledgments

This work was supported by the National Science Foundation under Grant No. 2027108. J.W.L. also acknowledges partial funding from the Burroughs Wellcome Fund Career Award at the Scientific Interface and NIGMS Grant No. 1R35GM142584-01.

References

[1]. Dura B, Chen MQ, Inan OT, Kovacs GTA, and Giovangrandi L, “High-frequency electrical stimulation of cardiac cells and application to artifact reduction,” IEEE Transactions on Biomedical Engineering, vol. 59, no. 5, pp. 1381–1390, 2012. [PubMed: 22345525]

[2]. Stoppel WL, Kaplan DL, and Black LD, “Electrical and mechanical stimulation of cardiac cells and tissue constructs,” Advanced Drug Delivery Reviews, vol. 96, pp. 135–155, 2016. [PubMed: 26232525]

[3]. Ronchi S, Fiscella M, Marchetti C, Viswam V, Müller J, Frey U, and Hierlemann A, “Single-cell electrical stimulation using CMOS-based high-density microelectrode arrays,” Frontiers in Neuroscience, vol. 13, 2019.

[4]. Heer F, Hafizovic S, Franks W, Blau A, Ziegler C, and Hierlemann A, “CMOS microelectrode array for bidirectional interaction with neuronal networks,” IEEE Journal of Solid-State Circuits, vol. 41, no. 7, pp. 1620–1629, 2006.

[5]. Lopez CM, Chun HS, Berti L, Wang S, Putzeys J, Van Den Bulcke C, Weijers J-W, Firrincieli A, Reumers V, Braeken D, and Van Helleputte N, “A 16384-electrode 1024-channel multimodal cmos mea for high-throughput intracellular action potential measurements and impedance spectroscopy in drug-screening applications,” in 2018 IEEE International Solid - State Circuits Conference - (ISSCC), 2018, pp. 464–466.

[6]. Eversmann B, Lambacher A, Gerling T, Kunze A, Fromherz P, and Thewes R, “A neural tissue interfacing chip for in-vitro applications with 32k recording / stimulation channels on an active area of 2.6 mm2,” in 2011 Proceedings of the ESSCIRC (ESSCIRC), 2011, pp. 211–214.

[7]. Shaik FA, Ihida S, Ikeuchi Y, Tixier-Mita A, and Toshiyoshi H, “Tft sensor array for real-time cellular characterization, stimulation, impedance measurement and optical imaging of in-vitro neural cells,” Biosensors and Bioelectronics, vol. 169, p. 112546, 2020.

[8]. Dragas J, Viswam V, Shadmani A, Chen Y, Bounik R, Stettler A, Radivojevic M, Geissler S, Obien MEJ, Müller J, and Hierlemann A, “In vitro multi-functional microelectrode array featuring 59 760 electrodes, 2048 electrophysiology channels, stimulation, impedance measurement, and neurotransmitter detection channels,” IEEE Journal of Solid-State Circuits, vol. 52, no. 6, pp. 1576–1590, 2017. [PubMed: 28579632]

[9]. Abbott J, Ye T, Krenek K, Gertner RS, Ban S, Kim Y, Qin L, Wu W, Park H, and Ham D, “A nanoelectrode array for obtaining intracellular recordings from thousands of connected neurons,” Nature biomedical engineering, vol. 4, no. 2, pp. 232–241, 2020.

[10]. Ballini M, Müller J, Livi P, Chen Y, Frey U, Stettler A, Shadmani A, Viswam V, Jones IL, Jäackel D, Radivojevic M, Lewandowska MK, Gong W, Fiscella M, Bakkum DJ, Heer F, and Hierlemann A, “A 1024-channel CMOS microelectrode array with 26,400 electrodes for recording and stimulation of electrogenic cells in vitro,” IEEE Journal of Solid-State Circuits, vol. 49, no. 11, pp. 2705–2719, 2014. [PubMed: 28502989]

[11]. Krawczyk K, Xue S, Buchmann P, Charpin-El-Hamri G, Saxena P, Hussherr M-D, Shao J, Ye H, Xie M, and Fussenegger M, “Electro-genetic cellular insulin release for real-time glycemic control in type 1 diabetic mice,” Science, vol. 368, no. 6494, pp. 993–1001, 2020. [PubMed: 32467389]

[12]. Abedin-Do A, Zhang Z, Douville Y, Méthot M, and Rouabhia M, “Effect of electrical stimulation on diabetic human skin fibroblast growth and the secretion of cytokines and growth factors involved in wound healing,” Biology, vol. 10, no. 7, 2021.

[13]. Abbott J, Mukherjee A, Wu W, Ye T, Jung HS, Cheung KM, Gertner RS, Basan M, Ham D, and Park H, “Multi-parametric functional imaging of cell cultures and tissues with a CMOS microelectrode array,” Lab on a Chip, vol. 22, no. 7, pp. 1286–1296, 2022. [PubMed: 35266462]

[14]. Comerci CJ, Gillman AL, Galera-Laporta L, Gutierrez E, Groisman A, Larkin JW, Garcia-Ojalvo J, and Süel GM, “Localized electrical stimulation triggers cell-type-specific proliferation in biofilms,” Cell Systems, 2022.

[15]. Nguyen BH, Takahashi CN, Gupta G, Smith JA, Rouse R, Berndt P, Yekhanin S, Ward DP, Ang SD, Garvan P et al. , “Scaling DNA data storage with nanoscale electrode wells,” Science advances, vol. 7, no. 48, p. eabi6714, 2021. [PubMed: 34818035]

[16]. Jung HS, Jung W-B, Wang J, Abbott J, Horgan A, Fournier M, Hinton H, Hwang Y-H, Godron X, Nicol R, Park H, and Ham D, "CMOS electrochemical pH localizer-imager," Science Advances, vol. 8, no. 30, p. eabm6815, 2022. [PubMed: 35895813]

[17]. Ghadami O, Lu H, Chan M, Tan M, Chung S, Lee SH, Holden MT, de Ridder R, Merriman B, and Hall DA, "Helix: An electrochemical CMOS DNA synthesizer," in 2022 IEEE Symposium on VLSI Technology and Circuits (VLSI Technology and Circuits). IEEE, 2022, pp. 66–67.

[18]. Hu K, Arcadia CE, and Rosenstein JK, "A large-scale multimodal CMOS biosensor array with 131,072 pixels and code-division multiplexed readout," IEEE Solid-State Circuits Letters, vol. 4, pp. 48–51, 2021.

[19]. Jung D, Junek GV, Park JS, Kumashi SR, Wang A, Li S, Grijalva SI, Fernandez N, Cho HC, and Wang H, "A CMOS 21 952-pixel multi-modal cell-based biosensor with four-point impedance sensing for holistic cellular characterization," IEEE Journal of Solid-State Circuits, vol. 56, no. 8, pp. 2438–2451, 2021.

[20]. Widdershoven F, Cossettini A, Laborde C, Bandiziol A, van Swinderen PP, Lemay SG, and Selmi L, "A CMOS pixelated nanocapacitor biosensor platform for high-frequency impedance spectroscopy and imaging," IEEE transactions on biomedical circuits and systems, vol. 12, no. 6, pp. 1369–1382, 2018. [PubMed: 30059320]

[21]. Chi T, Park JS, Butts JC, Hookway TA, Su A, Zhu C, Styczynski MP, McDevitt TC, and Wang H, "A multi-modality CMOS sensor array for cell-based assay and drug screening," IEEE Transactions on Biomedical Circuits and Systems, vol. 9, no. 6, pp. 801–814, 2015. [PubMed: 26812735]

[22]. Tedjo W and Chen T, "An integrated biosensor system with a high-density microelectrode array for real-time electrochemical imaging," IEEE Transactions on Biomedical Circuits and Systems, vol. 14, no. 1, pp. 20–35, 2020. [PubMed: 31751250]

[23]. Kumashi SR, Jung D, Park J, Sanz ST, Grijalva S, Wang A, Li S, Cho HC, Ajo-Franklin CM, and Wang H, "A CMOS multi-modal electrochemical and impedance cellular sensing array for massively paralleled exoelectrogen screening," IEEE Transactions on Biomedical Circuits and Systems, vol. 15, no. 2, pp. 221–234, 2021. [PubMed: 33760741]

[24]. Shadmani A, Viswam V, Chen Y, Bounik R, Dragas J, Radivojevic M, Geissler S, Sitnikov S, Müller J, and Hierlemann A, "Stimulation and artifact-suppression techniques for in vitro high-density microelectrode array systems," IEEE Transactions on Biomedical Engineering, vol. 66, no. 9, pp. 2481–2490, 2019. [PubMed: 30605090]

[25]. Arcadia CE, Hu K, Epstein S, Wanunu M, Adler A, and Rosenstein JK, "CMOS electrochemical imaging arrays for the detection and classification of microorganisms," in 2021 IEEE International Symposium on Circuits and Systems (ISCAS). IEEE, 2021, pp. 1–5.

[26]. Hu K, Kennedy E, and Rosenstein JK, "High frequency dielectric spectroscopy array with code division multiplexing for biological imaging," in 2019 IEEE Biomedical Circuits and Systems Conference (BioCAS). IEEE, 2019, pp. 1–4.

[27]. Hu K, Arcadia CE, and Rosenstein JK, "Super-resolution electrochemical impedance imaging with a 100× 100 CMOS sensor array," in 2021 IEEE Biomedical Circuits and Systems Conference (BioCAS). IEEE, 2021, pp. 1–4.

[28]. Hu K, Ho J, and Rosenstein JK, "Super-resolution electrochemical impedance imaging with a 512× 256 CMOS sensor array," IEEE Transactions on Biomedical Circuits and Systems, 2022.

[29]. Hu K, Arcadia CE, and Rosenstein JK, "A fringe field shaping CMOS capacitive imaging array," in 2021 IEEE Sensors, 2021, pp. 1–4.

[30]. Hu K, Incandela J, Lian X, Larkin JW, and Rosenstein JK, "A 13.1 mm2 512× 256 multimodal CMOS array for spatiochemical imaging of bacterial biofilms," in 2022 IEEE Custom Integrated Circuits Conference (CICC). IEEE, 2022, pp. 1–2.

[31]. Hu K, Lian X, Dai S, and Rosenstein JK, "Low noise CMOS ISFETs using in-pixel chopping," in 2019 IEEE Biomedical Circuits and Systems Conference (BioCAS). IEEE, 2019, pp. 1–4.

[32]. Tsai D, Sawyer D, Bradd A, Yuste R, and Shepard KL, "A very large-scale microelectrode array for cellular-resolution electrophysiology," Nature Communications, vol. 8, no. 1, pp. 1–11, 2017.

[33]. Rothe J, Frey O, Madangopal R, Rickus J, and Hierlemann A, "Robust functionalization of large microelectrode arrays by using pulsed potentiostatic deposition," Sensors, vol. 17, no. 1, 2017.

[34]. Bozzini B, Pietro De Gaudenzi G, and Mele C, “A SERS investigation of the electrodeposition of ag–au alloys from free-cyanide solutions,” Journal of Electroanalytical Chemistry, vol. 563, no. 1, pp. 133–143, 2004.

[35]. Matsuura K, Yamanishi Y, Guan C, and Yanase S, “Control of hydrogen bubble plume during electrolysis of water,” Journal of Physics Communications, vol. 3, no. 3, p. 035012, mar 2019.

[36]. Canty M, Luke-Marshall N, Campagnari A, and Ehrensberger M, “Cathodic voltage-controlled electrical stimulation of titanium for prevention of methicillin-resistant staphylococcus aureus and acinetobacter baumannii biofilm infections,” Acta Biomaterialia, vol. 48, pp. 451–460, 2017. [PubMed: 27890730]

[37]. Obata K, van de Krol R, Schwarze M, Schomäcker R, and Abdi FF, “In situ observation of pH change during water splitting in neutral pH conditions: impact of natural convection driven by buoyancy effects,” Energy Environ. Sci, vol. 13, pp. 5104–5116, 2020.

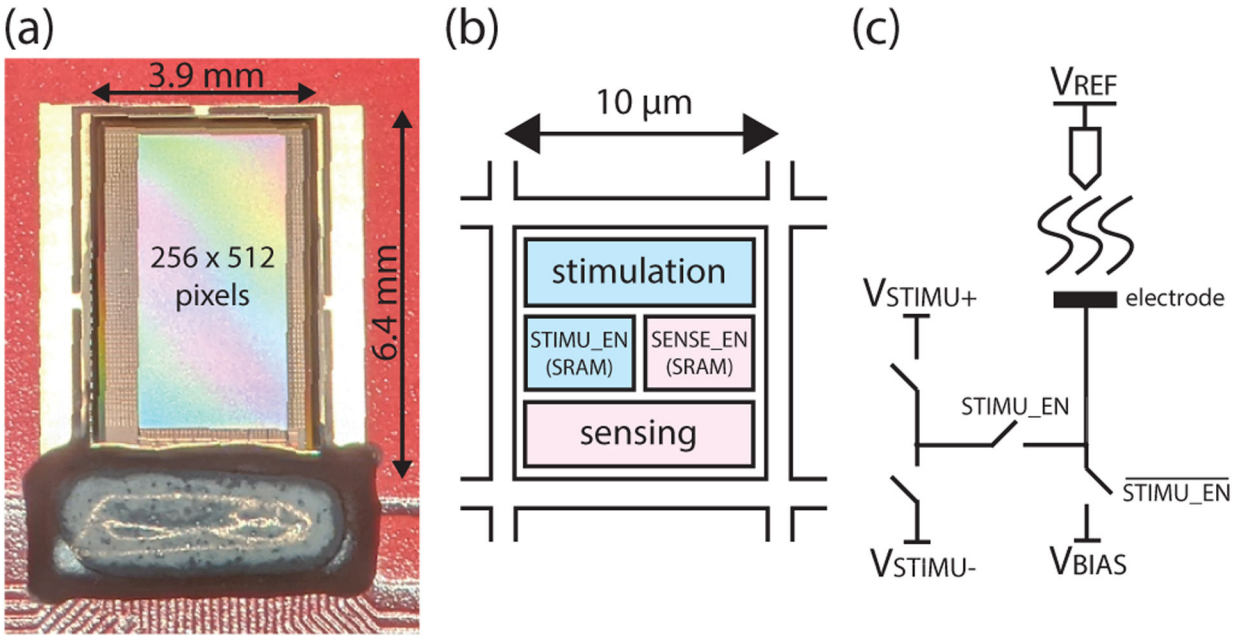

Fig. 1.

(a) An image of the CMOS microelectrode array. (b) Each pixel can be used for either stimulation or sensing, selected by in-pixel SRAM. (c) Simplified schematic of the programmable stimulation switches contained in each pixel.

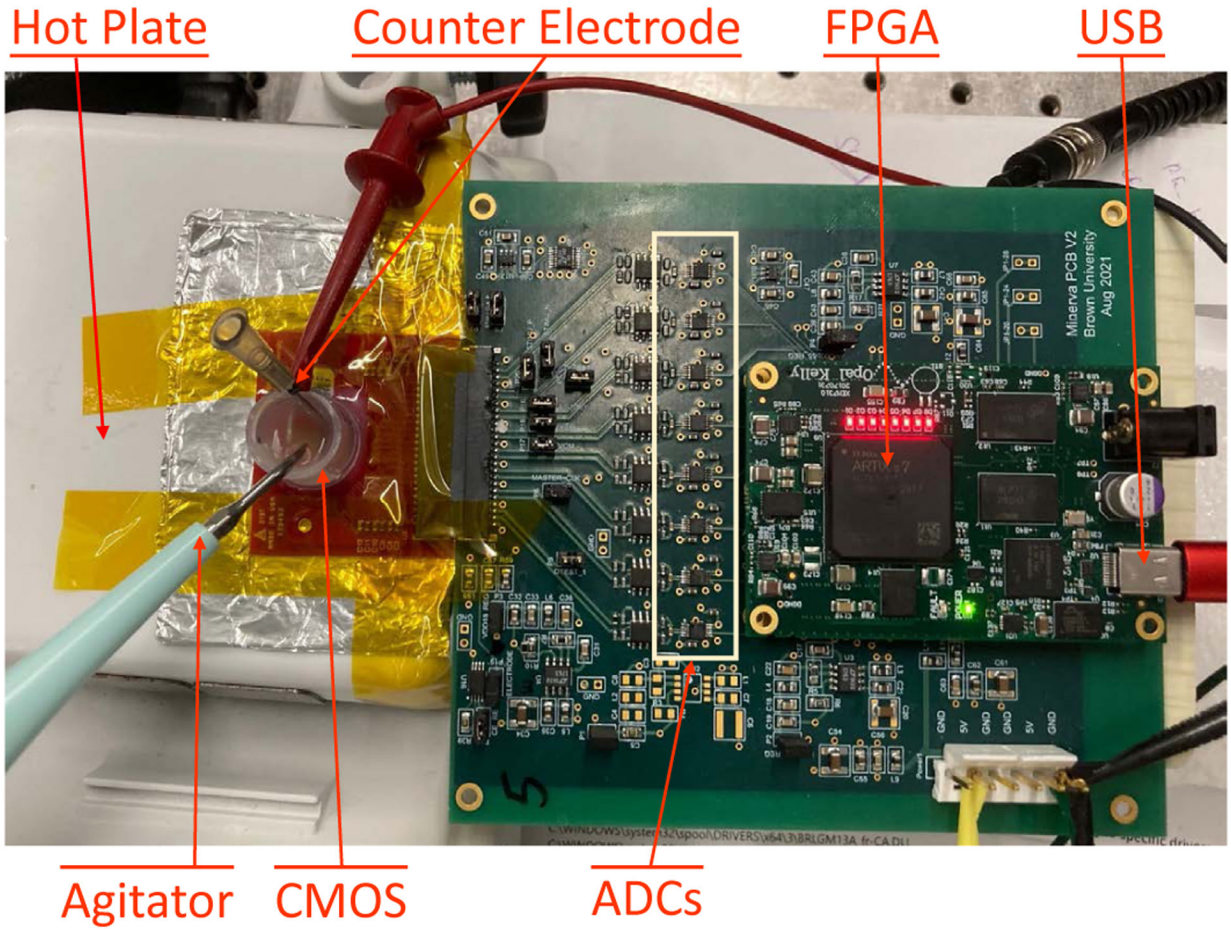

Fig. 2.
The experimental setup for gold electroplating on the CMOS microelectrode array.

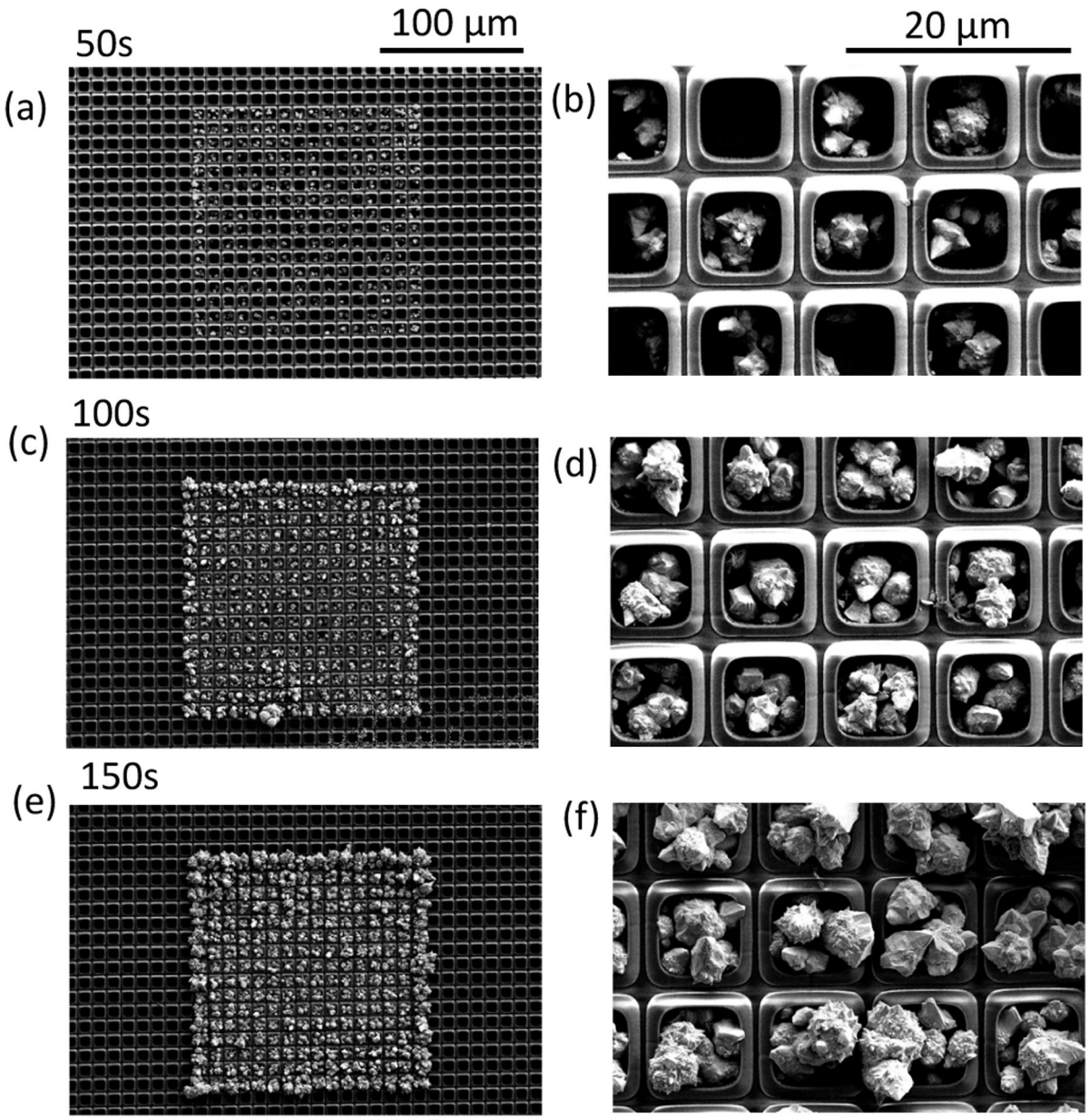

Fig. 3.

The effect of total deposition time for electroplating gold varied from (a) 50 s, (c) 100 s (e) 150 s. The deposition pulse period was 1 s with 50% duty cycle. The scale bar in (a), (c), (e) corresponds to 100 µm. The magnified images of the corresponding deposition time are shown from (b), (d), (f) with the scale bar corresponding to 20 µm.

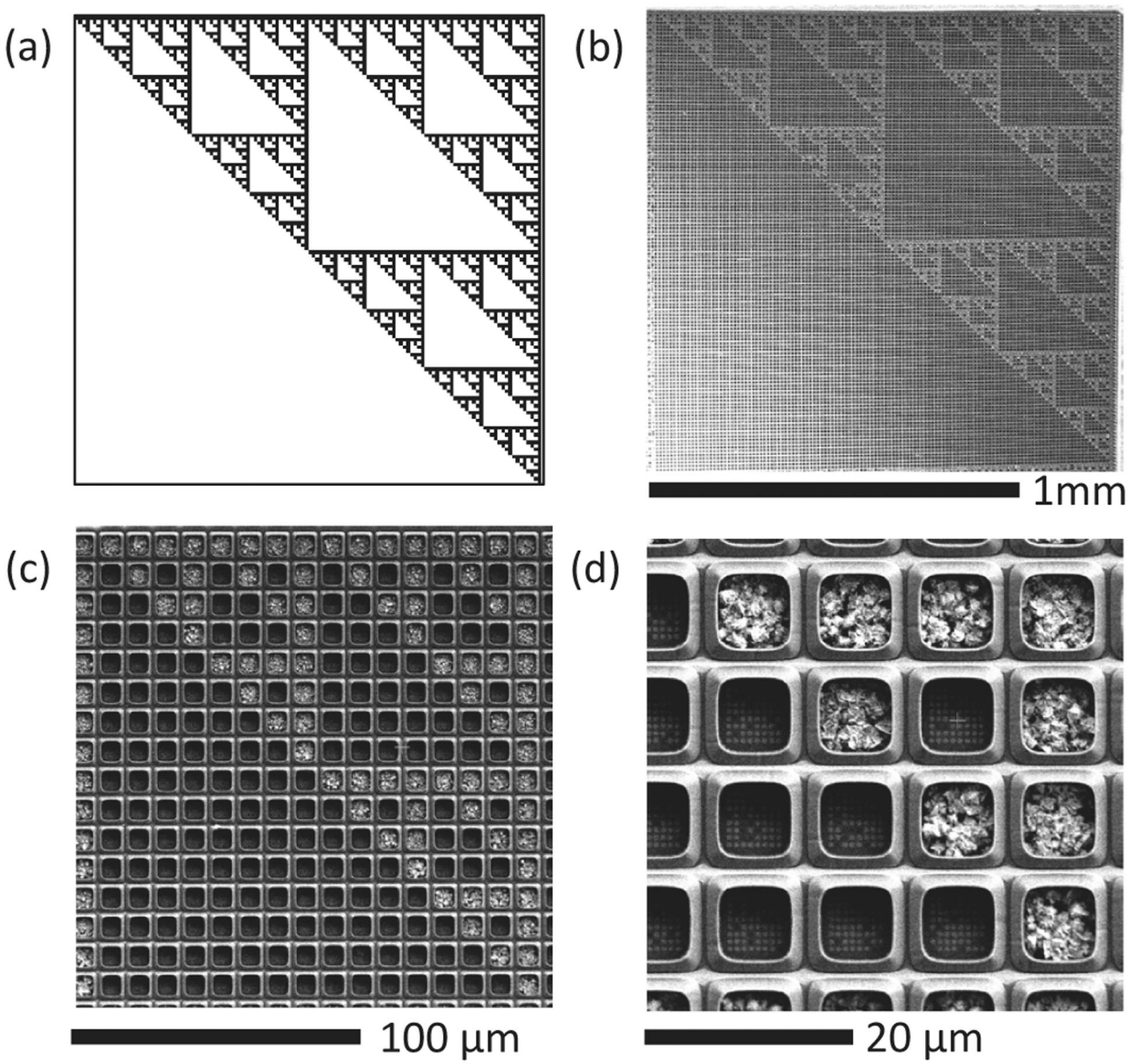

Fig. 4.

(a) A Sierpinski fractal pattern used to program stimulating (dark) and non-stimulating pixels (white). (b) An FESEM image of the microelectrode array with gold electrodeposition in the Sierpinski pattern. (c) – (f) SEM images of the same micro-patterned array at increasing magnification.

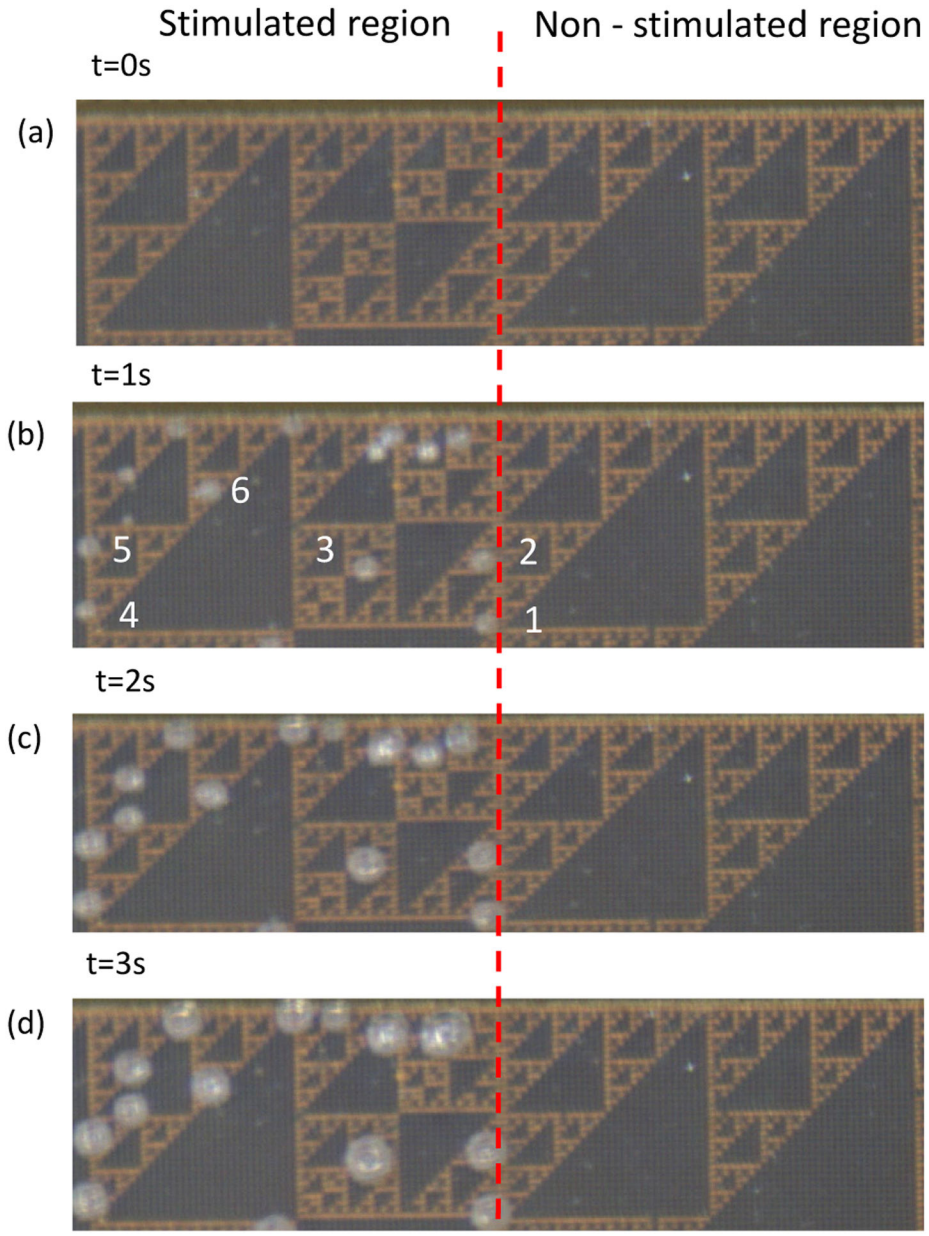

Fig. 5.

(a) The left half of the patterned CMOS microelectode array is stimulated to carry out electrolysis of water. (b) The bubbles marked with numbers 1–6 in are monitored for growth against time. (b) – (d) The bubbles grow steadily with time.

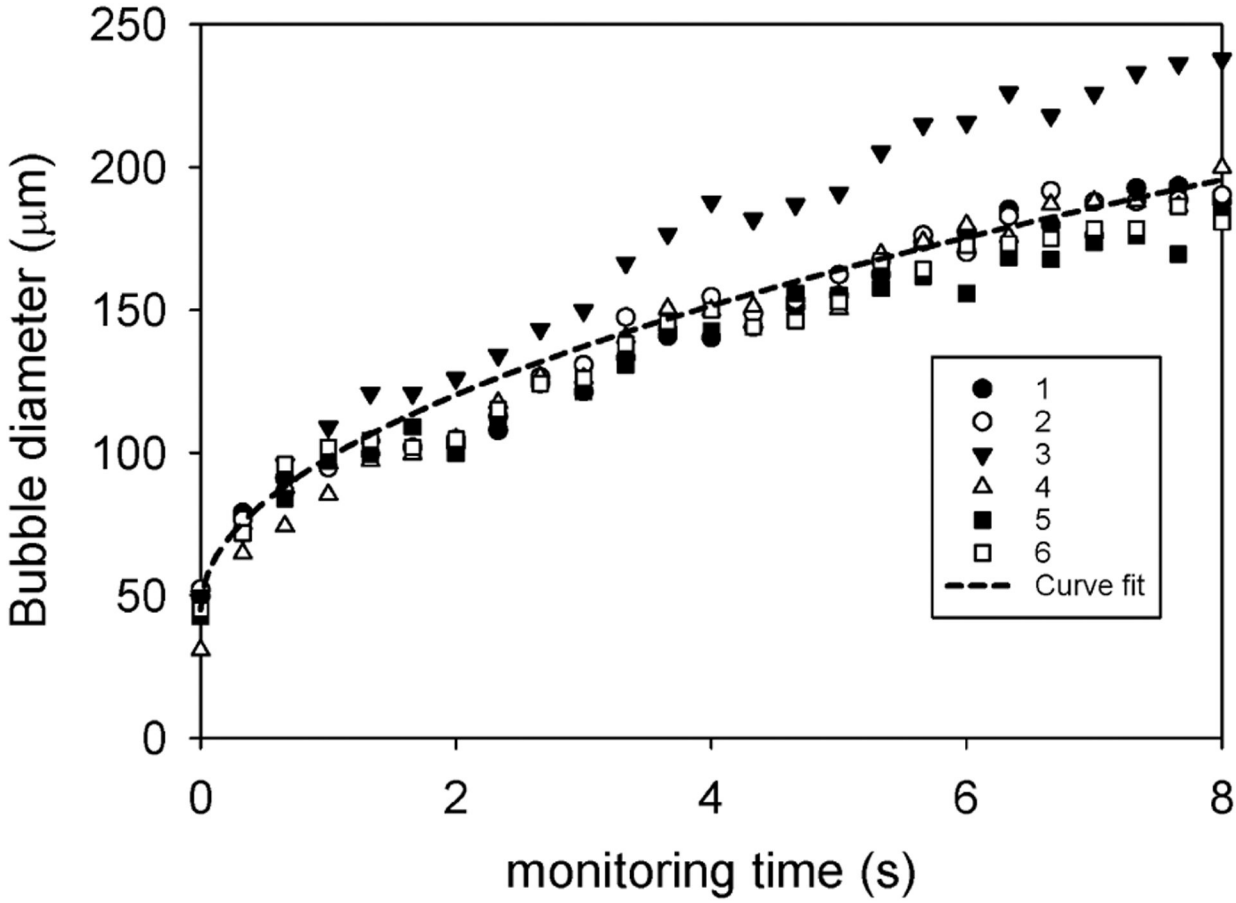

Fig. 6.

The growth of six bubbles are monitored beginning at time $t = 1$ sec (annotated in Fig. 5(b)). The trendline is a global fit to Eq. 2 with an average initial bubble size of 45 μm.

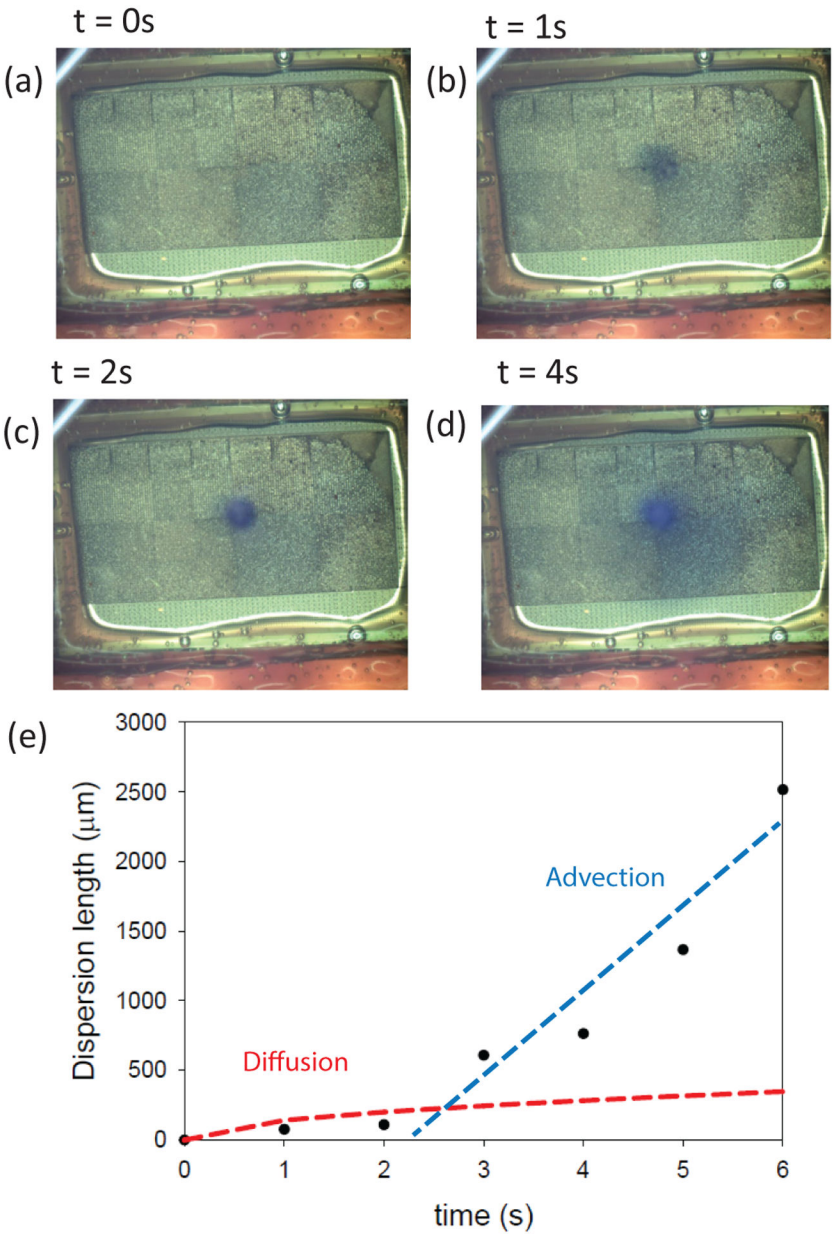

Fig. 7.

(a) - (d) The spatio-temporal variation of pH is visualized using a pH indicator dye (bromothymol blue) when an array of 50 × 50 pixels at the center of the chip is stimulated. (e) The apparent dispersion radius of the pH change beyond the stimulated pattern is tracked versus the time elapsed from the start of the stimulus. Trendlines for diffusion ($\propto \sqrt{t}$) and advection ($\propto t$) are overlaid as guides to the eye.

TABLE I

Comparisons to the state of the art

	This Work	[32]	[8]	[6]	[10]	[5]
# of Pixels	131,072	65,536	59,760	32,768	26,400	16,384
Stimulation Channels	131,072	65,536	16	32,768	32	4,096
Pixel Size	10 × 10 μm^2	25.5 × 25.5 μm^2	13.5 × 13.5 μm^2	8.8 × 8.8 μm^2	17.5 × 17.5 μm^2	15 × 15 μm^2
Field of View	2.56 × 5.12 (13.1 mm^2)	6.53 × 6.53 (42.6 mm^2)	4.48 × 2.43 (10.9 mm^2)	2.28 × 1.14 (2.6 mm^2)	4 × 2 (8 mm^2)	0.48 × 0.48 × 16 (3.7 mm^2)
Electrode Materials	W/TiN/Au	Al/HfO_2/Au	Al/PtB	Pt	Al/Pt	Al/Ti/TiN
Technology Node	180 nm	180 nm	180 nm	500 nm	350 nm	130 nm